

Large oxygen excess in the primitive mantle could be the source of the Great Oxygenation Event

D. Andraut, M. Muñoz, G. Pesce, V. Cerantola, A. Chumakov, I. Kantor,
S. Pascarelli, R. Rüffer, L. Hennet

Supplementary Information

The Supplementary Information includes:

- Methods
- Table S-1 to S-3
- Figures S-1 to S-8
- Supplementary Information References

Methods

We probed the Fe behaviour in various mineral assemblages at pressure and temperature conditions typical of the lower mantle using X-ray absorption near edge spectroscopy (XANES) and synchrotron Mossbauer spectroscopy (SMS).

1. Starting materials

We used different types of starting material (Table S-1): (i) ferroperricite ($\text{Mg}_{0.8}\text{Fe}_{0.2}\text{O}$), (ii) a fine powder mixture of a natural enstatite with $\text{Fe}/(\text{Mg}+\text{Fe}) = 0.17$ mixed with Al_2O_3 to produce an Fe/Al ratio of 1 ($\text{Al}_{0.17}\text{-Mg}_{0.83}\text{Fe}_{0.17}\text{SiO}_3$), and (iii) three synthetic glasses with compositions typical of a chondritic mantle with two times more Fe, to improve the XANES signal; with ^{57}Fe , to improve the SMS signal; and without Al. For our chondritic-type composition (the sample probed by SMS, for example), we expect a mineral mixture composed of 75.3 %, 17.0 %, 7.7 % of Bg, Fp and CaSiO_3 perovskite (CaPv), respectively. The typical atomic Fe/(Mg+Fe) ratio is ~0.11. Glasses were prepared using the high temperature aerodynamic levitation technique associated with CO_2 laser heating (Hennet *et al.*, 2011). The gas mixture (Ar with less than 0.05 ppm of oxygen) was adjusted in order to obtain no metal Fe and a minimum of Fe^{3+} . We determined the $\text{Fe}^{3+}/\Sigma\text{Fe}$ ratio ($\#\text{Fe}^{3+}$) as 7-8 %, using Mossbauer spectroscopy (see below, Fig. S-5). For all compositions, powders were ground for several minutes in a glove bag with a flow of nitrogen just before loading the pressure chamber, in order to prevent water contamination.

2. Experimental methods

We used the membrane-type diamond anvil cell (DAC) mounted with diamonds with beveled culets with diameters from 250/300 to 75/300 μm , depending on the target pressure. Pre-indented Re-gaskets were drilled in the centre using a pulsed laser to a diameter of ~1/3 of the internal culet diameter. Pressures at 300 K were determined from the Raman-shift of the major peak of the diamond surface in contact with the sample. The sample pressure can increase during the laser heating (*e.g.*, ~5 GPa for heating to 2500 K) due to the effect of thermal pressure (Andraut *et al.*, 1998). Up to ~60 GPa, we sometimes used a thin layer of KCl between the sample and diamonds to minimise the axial temperature gradient within the sample. At higher pressures, we used no pressure medium, because the use of a KCl layer resulted in a significant deterioration of the XANES and SMS spectra. For XANES measurements, thin diamond anvils 1.6 mm in height were selected in order to reduce the X-ray absorption at the Fe K-edge energy (7112 eV). Also, we added a piece of KCl on the sample side in the gasket hole to allow measurement of the X-ray beam intensity



(I₀).

A similar strategy was used on both ID24 and ID18 beamlines for the laser heating. After the target pressure was achieved, we transformed the samples using two fibre lasers of 100 W, with available on-line systems (Kupenko *et al.*, 2012). For final laser alignments, we used optical lenses with focal lengths of 35 or 50 mm. We defocused lasers until the size of the hot spot on the sample was 10-15 μm . The sample temperature was monitored by thermal radiometry, and was progressively increased up to 2000, 2500 or 3500 K (Table S-2). At each pressure investigated, we slowly scanned the sample between the two lasers to anneal the whole sample volume, for about 30 minutes, before the lasers were quenched. For SMS measurements, we used one fresh sample per pressure condition. This procedure prevents potential problems associated with slow atomic diffusion between grains, once the starting material has already been transformed. For XANES measurements, each sample was recompressed and reheated to the maximum temperature over a pressure range of 30-40 GPa, before another sample was synthesised at a different pressure range (Table S-2). Some chemical segregation could occur during the scan of the laser spot on the sample. Increasing the Fp and Bg grain size might produce heterogeneities at the level of microns (Fig. 1). However, X-ray beams were significantly larger than the grain size, with FWHM of 5 μm and 10-15 μm in case of XANES and SMS, respectively. For XANES, we recorded maps on which measurements were averaged.

3. XANES results

3.1 Experimental methods. XANES hyperspectral mapping was performed at the Fe K-edge using dispersive spectroscopy at the ID24 beamline (ESRF) (Muñoz *et al.*, 2006). We used an Si(220) bent crystal polychromator that provides the best compromise between spectral resolution for pre-edge absorption peak analysis, X-ray flux and k-space extension. The polychromatic X-ray beam was focused to a $\sim 5 \times 5 \mu\text{m}^2$ spot at the sample location. The absorption spectrum $\mu(E)$ is equal to $\ln(I_0/I_1)$ where I_1 , and I_0 , are X-ray intensities recorded by the spatially resolved CCD detector through the sample position, and a piece of KCl, respectively. Both I_0 and I_1 were measured through diamonds. The DAC was rotated in the X-ray beam to remove diffraction peaks of diamonds from the energy range of interest. Acquisition time was a few minutes. To improve statistics and prevent potential artefacts related to grain growth and sample heterogeneity, we performed sample maps in the diamond anvil cell with a spatial resolution of $\sim 5 \times 5 \mu\text{m}^2$, on which the recorded XANES signals were averaged (Munoz *et al.*, 2008).

The basic methodology was similar to our previous work (Andrault *et al.*, 2010). However, the quality of measurements was much improved to the point that we could use the pre-edge features located around 7110-7115 eV (Fig. S-2) to refine the $\text{Fe}^{3+}/(\text{Fe}^{2+}+\text{Fe}^{3+})$ ratio ($\#\text{Fe}^{3+}$) in our samples *in situ* at high pressures. Fit to experimental pre-edge was performed between 7108 and 7118 eV using 3 pseudo-voigt peak-components with a fixed band width of 2 eV and a 50:50 Lorentz/Gaussian peak shape (Fig. S-4). The pre-edge centroid energy (PCE) was then calculated by summing each peak position weighted by its corresponding area fraction (Wilke *et al.*, 2001; Munoz *et al.*, 2013). The energy calibration requires the use of internal standards. In our study, we used olivine as a standard for the PCE, to match the value of (Wilke *et al.*, 2001). Also, in order to compare our results with previous PCE values reported for Bg (Boujibar *et al.*, 2016), we corrected their PCE value using their “internally consistent” siderite reference. In this way, all our PCE values are consistent with each other.

3.2 Fe partitioning between Bg and Fp. We first investigated the evolution of XANES features for two reference compounds, Fp ($\text{Mg}_{0.8}\text{Fe}_{0.2}\text{O}$) and Bg ($\text{Al}_{0.17}\text{Mg}_{0.83}\text{Fe}_{0.17}\text{SiO}_3$), upon compression to 104 GPa and 62 GPa, respectively (Fig. S-1). For Bg, we performed laser annealing to ~ 2500 K for several minutes after each pressure increment, to enable a potential evolution of the point-defect population (e.g., Fe^{3+} and oxygen vacancies) in the Bg lattice. The pressure evolution of XANES features is very compatible with previous work (Narygina *et al.*, 2009). The two reference compounds present well contrasted XANES shapes. Fp shows a well-structured XANES with several maxima and minima in the energy domain of ~ 90 eV available in this study. The energy position of the first peak at 7120-7125 eV is found to be independent of pressure, while other contributions shift to higher energies with increasing pressure (corresponding to a decrease in interatomic distance). The spin transition reported for Fe in Fp in the pressure range investigated (Badro *et al.*, 2003) does not produce any significant effect on XANES features. In contrast, the XANES shape of Bg is rounded and only mildly affected by pressure, at least up to 62 GPa. The difference in shape and pressure evolution of Bg and Fp XANES results facilitate the spectral deconvolution in our samples composed of a mixture of both phases (Munoz *et al.*, 2008; Narygina *et al.*, 2011).

We then investigated our two synthetic glasses with compositions typical to chondritic mantle, but with either two times more Fe or without Al (Tables S-1 and S-2). At each P-T condition, the spectral deconvolution was performed using a linear combination of XANES spectra of Fp and Bg recorded at a similar pressure (Fig. S-2) (Munoz *et al.*, 2008; Andrault *et al.*, 2010). It provides fractions of Fe located in Fp and Bg phases as a function of the experimental pressure and temperature. It yields the Fe partition coefficient between Bg and Fp ($K_{\text{Fe}^{\text{Bg/Fp}}} = X_{\text{Fe}^{\text{Bg}}} X_{\text{Mg}^{\text{Fp}}} / X_{\text{Mg}^{\text{Bg}}} X_{\text{Fe}^{\text{Fp}}}$), based on the molar ratio of Fp and Bg expected for each starting material. At low pressure, we observe significantly different $K_{\text{Fe}^{\text{Bg/Fp}}}$ for both samples, probably because they contain different amounts of Al and Fe (Fig. S-3). This effect has been systematically studied in the past at moderate pressures (Wood and Rubie, 1996). In contrast, the refined $K_{\text{Fe}^{\text{Bg/Fp}}}$ values plot close to each other for all samples above ~ 50 GPa. Overall, we observe a large decrease in $K_{\text{Fe}^{\text{Bg/Fp}}}$ with increasing pressure, which could be related to the change in spin of Fe in Fp (Badro *et al.*, 2004; Lin *et al.*, 2007). Our results suggest ~ 5 (+/- 1) times more Fe in Fp, compared to Bg, in the lower mantle for depths greater than ~ 1250 km.



3.3 Fe redox state. The PCEs of $(\text{Mg}_{0.8}\text{Fe}_{0.2})\text{O}$ Fp and $\text{Al}_{0.17}-(\text{Mg}_{0.83}\text{Fe}_{0.17}\text{SiO}_3)$ Bg references plot within the range of energy values typical of many Fe^{2+} - Fe^{3+} minerals (Wilke *et al.*, 2001) (Fig. 2). Our $\text{Mg}_{0.9}\text{Fe}_{0.1}\text{O}$ reference Fp contains almost exclusively Fe^{2+} . However, its PCE still plots at relatively high energy, in agreement with previous reports (Wilke *et al.*, 2001). Concerning our Bg reference compound, we performed an SMS analysis on the recovered sample and refined an $\#\text{Fe}^{3+}$ of 27(3) % (Fig. S-6).

With increasing pressure, PCEs of both Fp and Bg increase by 0.3–0.4 eV up to ~30 GPa, before they progressively decrease at higher pressure. The situation is complicated, however, because we lack knowledge about the pressure effect on the energy position and intensity of pre-edge features. At this stage, this means that our XANES measurements for the determination of the redox state in our samples remain qualitative. Still, we observe that Bg plots (i) at relatively higher energies, compared to Fp, most likely due to a higher Fe^{3+} -content in Bg (McCammon, 1997), and (ii) 2 to 3 times higher for integrated areas. The relatively high intensities are likely due to a less centrosymmetric site in Bg (the Fe-O_{12} dodecahedral site is highly distorted), compared to the Fe-O_6 octahedral site in Fp. Accordingly, when Fp and Bg coexist in a same sample, the Fe fraction located in the Bg should dominate the pre-edge features.

Both Fp and Bg reference compounds show a significant decrease in PCE with increasing the pressure (Fig. 2). This effect cannot be related to a change in $\#\text{Fe}^{3+}$ in Fp, because the sample was compressed at 300 K. Explanations for this pressure effect could be complex, because pre-edge features are related to intrinsic 1s–3d electronic transitions in Fe. For Bg, the pressure evolution is found to be parallel to that of Fp, suggesting a constant Fe^{3+} -content in the pressure range investigated, despite the laser annealing performed after each increment of pressure increase from 35 to 62 GPa.

For our two chondritic-type samples containing both Bg and Fp, PCEs are found at similar, or slightly higher, energies than observed for the Bg reference. One possible explanation for this is major partitioning of Fe^{2+} to Fp (Prescher *et al.*, 2014), which leaves Bg with a higher $\#\text{Fe}^{3+}$. Because Bg presents significantly more intense pre-edge features than Fp (Wilke *et al.*, 2001), it yields a higher PCE for the bulk sample. We also observe a global increase in the centroid energy with increasing pressure (Fig. 2). This observation contrasts with trends observed for the reference compounds, Fp and Bg, which excludes a decrease in the bulk $\#\text{Fe}^{3+}$ with increasing pressure in our chondritic-type samples.

4. SMS results

4.1 Experimental methods. SMS was performed with the Nuclear Resonance ID18 beamline (ESRF) using the (111) Bragg reflection of a $^{57}\text{FeBO}_3$ single crystal mounted on a Wissel velocity transducer driven with a sinusoidal wave form (Potapkin *et al.*, 2012). The crystal temperature was adjusted to achieve a maximum X-ray flux for an energy resolution of ~6 neV. Energy was tuneable over a range of about ± 0.6 μeV . The X-ray beam was focused to 15×10 μm^2 using two Kirkpatrick-Baez multilayer optics. The linewidth of the SMS and the absolute position of the center-shift (CS) was controlled before and after each measurement using a $\text{K}_2\text{Mg}^{57}\text{Fe}(\text{CN})_6$ reference single line absorber. The velocity scale was calibrated using 25 μm thick natural α -Fe foil. The average collection time was 4 to 10 hours for samples located inside the DAC.

A new sample was used at each experimental pressure. We recorded 8 SMS spectra of the glass upon compression to 123 GPa and several SMS spectra on 8 different samples transformed at high temperatures at pressures up to 142 GPa. The complete sample transformation was monitored based on (i) our knowledge of the minimum time required at 2500 K for the phase transformation (Andraut *et al.*, 2010) and (ii) the change with heating time of SMS features. For example, the main absorption peak of the compressed glass and the transformed sample plot around -0.5 mm/s or + 0.5 mm/s, respectively, at high pressures. At lower pressures, an intense contribution at a relative velocity position of 2–2.5 mm/s is present in the starting glass and not in the transformed sample (Fig. S-5). All SMS spectra which showed a mixture of the starting glass and transformed material were discarded.

All spectra were fitted using a full transmission integral with a normalized Lorentzian-squared source line-shape using the MossA software package (Prescher *et al.*, 2012). Previous articles have already investigated the typical Fe SMS signal in pure Bg (Kupenko *et al.*, 2014) and pure Fp (Kantor *et al.*, 2009) under pressure. For both phases, the central shift (CS) and the quadrupole splitting (QS) of various Fe atomic sites were reported as a function of pressure up ~80 GPa. We have relied strongly on these previous studies to deconvolve our SMS patterns recorded for equilibrated mixtures of Bg (or Post-Bg) and Fp.

4.2 Spin transition in Fp. All our SMS patterns could be fitted by a sum of 5 different Fe contributions: high-spin Fe^{2+} and low-spin Fe^{2+} in Fp (Kantor *et al.*, 2009), high-spin Fe^{2+} with low-QS, intermediate-spin Fe^{2+} and high-spin Fe^{3+} in Bg (McCammon *et al.*, 2008; Kupenko *et al.*, 2014) (Fig. S-7). Due to a large number of parameters, we first adjusted the fraction of each Fe contribution fixing all CS and QS values to those reported in the literature. We then optimised the CS and QS values. The first observation is a clear change in both CS and QS for Fe^{2+} in Fp, at between 51 and 77 GPa (Fig. S-8), associated with the progressive HS to LS transition of the Fe in Fp at high temperature (Lin *et al.*, 2007). This transition pressure is compatible with a $\text{FeO}/(\text{MgO}+\text{FeO})$ ratio between 0.2 and 0.5 (Fei *et al.*, 2007). It is compatible with an FeO-content in Fp of 25–30 %, which we can estimate based on the relative intensity between the different Fe components present in the SMS spectrum of the sample synthesized at ~77 GPa (see below for the method to calculate this FeO-content). All other CS and QS parameters follow a smooth evolution with pressure which is compatible with previous works (Kantor *et al.*, 2009; Kupenko *et al.*, 2014). In particular, SMS patterns fit well with two



Fe²⁺ contributions in Bg, HS and IS, with a significant amount of IS Fe²⁺ above ~30 GPa.

One could argue that artefacts arise in our study, due to the fact that we neglected a potential Fe³⁺ for Fp. However, such an Fe-contribution is not observed in our SMS patterns. In addition, although it is reported in one EELS study that uses the most oxidised starting material (Prescher *et al.*, 2014), it is not observed in the other one (Piet *et al.*, 2016), nor in another report using EELS on quenched large volume press samples (Irifune *et al.*, 2010).

4.3 Fe-partitioning between Fp and Bg. We observe a progressive increase in Fe²⁺-content in Fp (combining HS and LS contributions) up to a pressure of ~80 GPa (Fig. 3b) which is related to the spin transition described above. At an experimental pressure of ~50 GPa, for example, the sum of Fe contributions in Bg and Fp indicates that 70 % of the Fe is located in Bg and 30 % in Fp (Fig. 3a). Due to the starting material composition (75.3 % Bg and 17.0 % Fp, Table S-1), it yields a $K_{\text{Fe}^{\text{Bg/Fp}}}$ of ~0.5. This value, as well as other $K_{\text{Fe}^{\text{Bg/Fp}}}$ values calculated in the same way based on all our SMS results, are in good agreement with our XANES results (Fig. S-3). In the pressure field where post-Bg becomes a major component, we calculate a $K_{\text{Fe}^{\text{Bg/Fp}}}$ of ~0.39(3) and ~0.22(3) for sample synthesis at ~2500 K and ~3500 K, respectively. The higher K_D value measured at 142 GPa, relative to that at lower pressures, suggests that Fe is less incompatible in post-Bg, in agreement with previous work (Murakami *et al.*, 2005).

4.4 Fe redox state. At pressures below 30-35 GPa, we found a bulk #Fe³⁺ of ~10-15 % (Fig. 3a), which fits well with the high-spin Fe³⁺ contribution in Bg (Fig. S-7). This #Fe³⁺ is comparable to the 15 % (McCammon *et al.*, 2008) and 21 % (Boujibar *et al.*, 2016) given for the Bg lattice, but it plots significantly lower than other values of #Fe³⁺ for Bg of up to 30 % or even 42 % in pyrolitic samples (McCammon *et al.*, 2008). Our data set also plot significantly lower than a previous study performed using the same experimental tools on a single phase of Bg pre-synthesized using the large volume press (LVP) (Kupenko *et al.*, 2015). Al-bearing garnets are stable below 30-35 GPa (e.g. Irifune *et al.*, 1996)). Their potential presence in our low-pressure samples would significantly decrease the Al-content in Bg and would in turn decrease its #Fe³⁺ (Fig. 3b). In our LH-DAC experiments, we do not have high enough resolution to further constraint the mantle #Fe³⁺ between 24 and 30-35 GPa, compared to previous LVP works. Nevertheless, it is clear that one should expect (i) a relatively low #Fe³⁺ in Bg (typically 10 to 25 %) in the presence of garnet and (ii) a higher #Fe³⁺ in Bg (#Fe³⁺ of 25-30%, (Kupenko *et al.*, 2015)) in the absence of garnet. We note that the uncertainty concerning the mantle #Fe³⁺ between 24 and 30-35 GPa does not have a significant impact on the main conclusions of our work.

In the pressure range between ~40 and 115 GPa, the bulk #Fe³⁺ remains relatively constant at ~20 % (Fig. 3a). Due to a progressive decrease in Fe²⁺-content in Bg, the #Fe³⁺ in Bg increases from ~25 % to ~35 % over this pressure range (Fig. 3b). Above 40 GPa, there is a very good agreement between our data set and the values presented by (Kupenko *et al.*, 2015), which were obtained using a very similar approach. In contrast, other previous data sets plot sometimes above, sometimes below our experimental trend. Differences in experimental conditions may explain the observed discrepancies: (i) A relatively high #Fe³⁺ was reported below ~80 GPa in some studies that used relatively oxidised starting materials (#Fe³⁺ of 25 % and 42 % in (Piet *et al.*, 2016) and (Prescher *et al.*, 2014), respectively), compared to the #Fe³⁺ of 7-8 % in our glass starting material. (ii) A relatively low #Fe³⁺ was measured in Bg samples synthesised between 50 and 70 GPa (Shim *et al.*, 2017). However, this is the pressure range where Fe²⁺ undergoes a change in spin in Fp, favoring the partitioning of Fe²⁺ to the Fp phase when Fp and Bg coexist at mantle-relevant compositions. In the absence of Fp, the Fe²⁺ remains in Bg leading to a relatively low #Fe³⁺. (iii) The very high #Fe³⁺ reported by (Sinmyo *et al.*, 2011) are difficult to explain. The great care put in to controlling the redox state of starting materials in this latter study may have been undermined by the use of gels, which can be high in water content.

In the pressure field where post-Bg becomes a major component, we measure a significantly higher bulk #Fe³⁺, 28 % to 32 %, compared to at lower pressure. This mantle #Fe³⁺ corresponds to an #Fe³⁺ of a mixture of Bg and post-Bg close to 50 % (Fig. 3).



Supplementary Tables

Table S-1 Composition of the starting material.

Sample Material	Fp-20 Synthetic	Al-En Powder-mix	CI-NoAl Glass	CI-2Fe Glass	CI- ⁵⁷ Fe Glass
SiO ₂	-	48.82	50.10	44.87	50.46
TiO ₂	-	-	0.21	0.19	0.05
Al ₂ O ₃	-	14.08	0.00	3.73	4.14
Cr ₂ O ₃	-	-	0.31	0.28	0.01
FeO	30.83	9.92	7.50	13.43	7.68
MgO	69.17	27.18	35.42	31.72	33.51
CaO	-	-	5.94	5.32	3.63
Na ₂ O	-	-	0.52	0.47	0.53
Al/Fe	0	1	0	0.39	0.76
Bg/(Bg+Fp)	0	1	0.72	0.67	0.82

En, Fp and Bg stand for enstatite, ferropicricle and bridgmanite, respectively. The expected Bg/(Bg+Fp) ratio is calculated including all Al₂O₃ in the Bg phase with the coupled substitution mechanism.

Table S-2 Summary of experimental runs.

Sample	Analyt. Tech.	P-range (GPa)	Strategy	Temperature (K)
Fp-20	XANES	15-104	A	300
Al-En	XANES	35-62	B	2500
CI-NoAl	XANES	33-66	B	2500
CI-2Fe	XANES	46-122	B	2500
CI- ⁵⁷ Fe	SMS	0-123	A	300
CI- ⁵⁷ Fe	SMS	23-142	C	2000 to 3500

Experimental conditions A, B, and C correspond to compression at 300 K, compression with laser annealing at each pressure step, and synthesis of a new sample at each pressure step, respectively.



Table S-3 List of the SMS parameters.

Press. GPa	Temp. K	Fp: Fe ²⁺ HS and LS				Bg: Fe ²⁺ HS and Low QS				Bg: Fe ³⁺ HS				Bg: Fe ²⁺ IS				Chi-square
		CS	QS	FWHM	Int.	CS	QS	FWHM	Int.	CS	QS	FWHM	Int.	CS	QS	FWHM	Int.	
23	2000	0.936	1.04	0.574	15.71	1.097	2.228	0.9	67.9	0.288	1.162	0.4	9.78	1.205	3.505	0.35	6.611	0.73
32	2000	0.889	1.15	0.509	17.5	1.042	2.269	0.795	64.74	0.36	1	0.4	15.17	1.1	3.6	0.35	2.585	1.062
32	2500	0.86	1.15	0.577	21.81	1.028	2.305	0.791	60.65	0.36	1	0.4	14.94	1.1	3.6	0.35	2.602	1.209
42	2500	0.866	1.14	0.42	27.64	1.079	2.211	0.848	54.22	0.36	1	0.4	16.38	1.05	3.7	0.35	1.762	1.105
42	3500	0.852	1.152	0.495	24.56	1.141	2.224	0.85	50.85	0.346	0.989	0.4	21.16	1.05	3.822	0.35	3.424	0.93
50	2500	0.824	0.936	0.45	31.08	1.039	2.029	0.903	44.77	0.241	1	0.4	18.47	1.05	3.8	0.35	5.678	1.8
51	2500	0.909	1.023	0.721	26.17	1.084	2.326	0.85	50.31	0.304	1.174	0.4	21	1.122	3.85	0.35	2.522	1.13
77	2500	0.436	0.278	0.45	44.61	1	2.2	0.903	26.19	0.166	1.2	0.4	18.02	0.982	4.003	0.35	11.19	0.58
115	2500	0.358	0.221	0.45	50.5	1	2.2	0.903	25.79	0.166	1.245	0.45	18.98	0.982	4	0.35	4.736	0.63
142	2500	0.326	0.25	0.5	33.68	1.045	2.5	0.434	23.05	0.131	1.471	0.5	31.59	0.98	4.15	0.35	11.68	1.425
142	3500	0.392	0.25	0.5	44.2	1.069	2.309	0.434	15.77	0.2	1.3	0.5	27.49	0.98	4.15	0.35	12.53	0.725

Abbreviations are for Pressure (Press.), Temperature (Temp.), High-Spin (HS), Low-spin (LS), Intermediate spin (IS), Central shift (CS), quadrupole splitting (QS), Full width half maximum (FWHM), Relative intensity (Int.). For Fp, we present the results for HS and LS Fe²⁺ in the same column.

Supplementary Figures

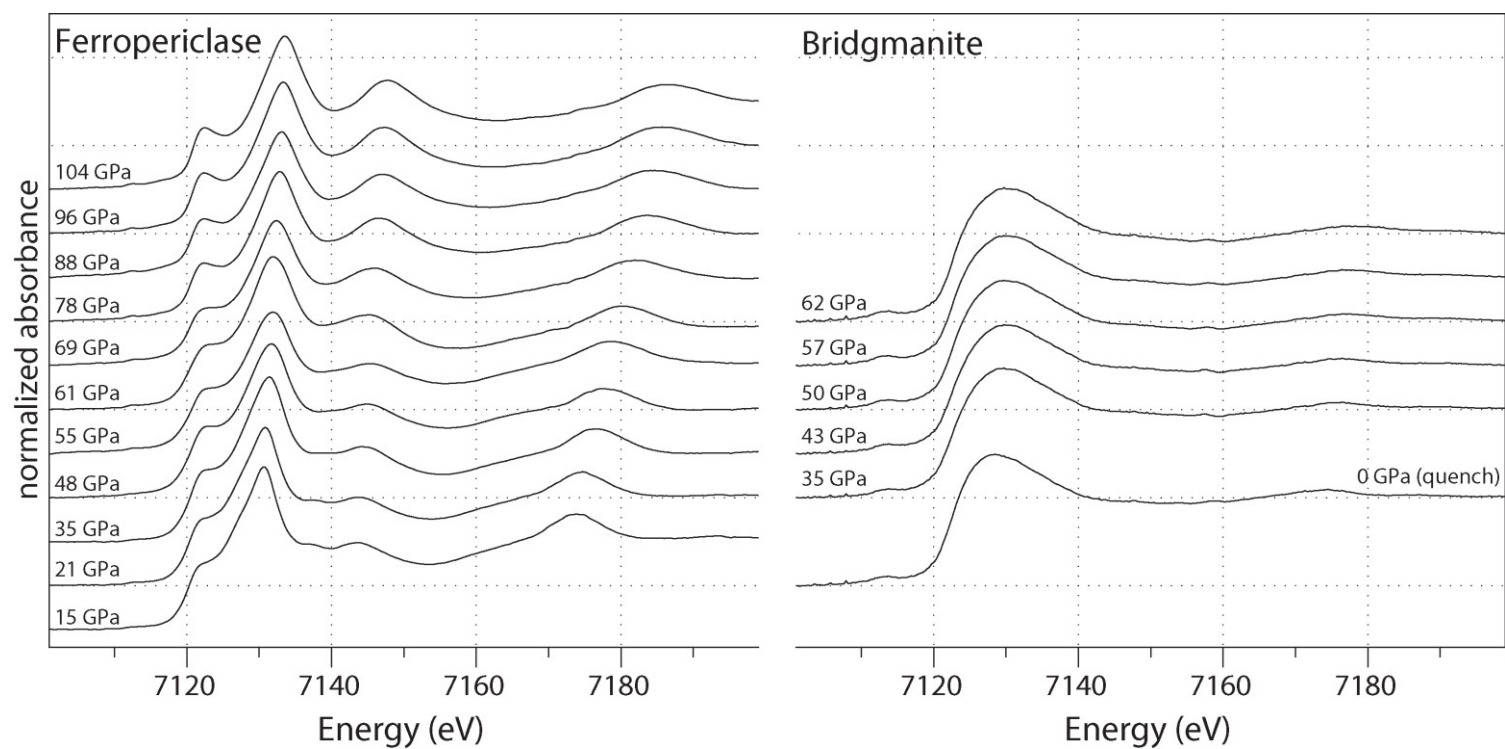


Figure S-1 XANES spectra of Fp and Bg standards upon compression to 104 and 62 GPa, respectively. Reference compounds consist in $\text{Mg}_{0.8}\text{Fe}_{0.2}\text{O}$ Fp (**left**) and $\text{Al}_{0.17}\text{-(Mg}_{0.83}\text{Fe}_{0.17}\text{SiO}_3)$ Bg (**right**). The Fe K-edge absorption spectra are all normalised.

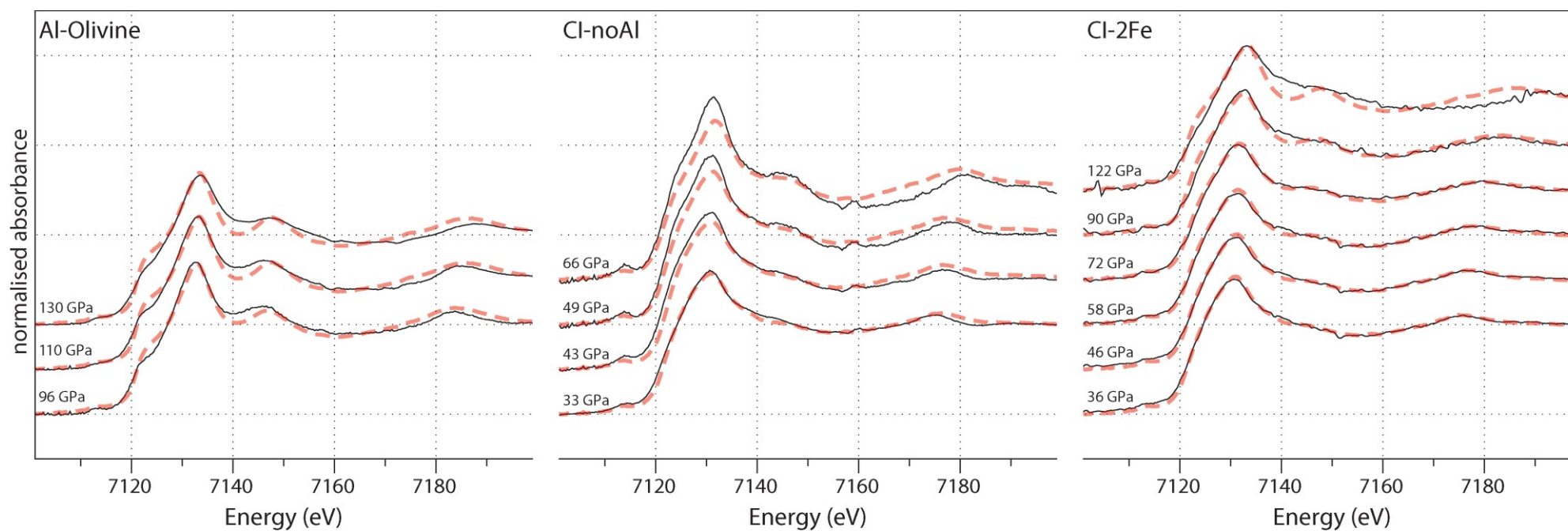


Figure S-2 Deconvolution of XANES spectra of our samples. Sample compositions are typical chondritic-type mantle, with no Al (CI-noAl, left) or two times more Fe (CI-2Fe, right) (see Tables S-1 and S-2). We report experimental spectra (black lines) together with their respective fits (red dashed lines) based on the linear combination of reference spectra (Fp and Bg, from Fig. S-1) taken at similar pressures. We used the pre-edge features located around 7110-7115 eV to qualitatively refine the $\#Fe^{3+}$ in our samples (see Fig. S-4).

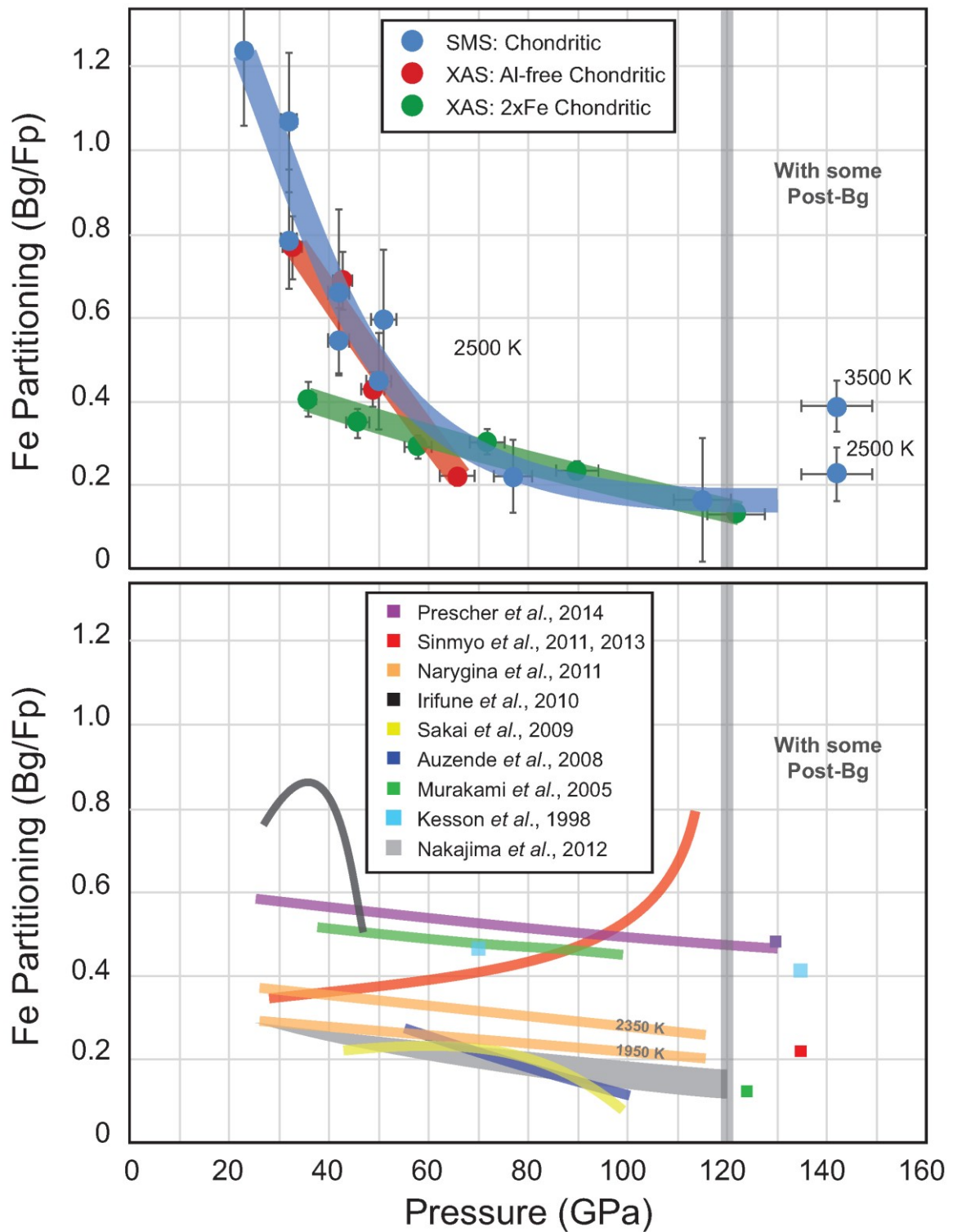


Figure S-3 Fe partition coefficient ($K_{Fe}^{Bg/Fp}$) between Bg and Fp. Our experimental data (top frame) show a large decrease of $K_{Fe}^{Bg/Fp}$ with increasing pressure up to the pressure of ~60 GPa, which can be explained by the spin transition of Fe in Fp (Lin *et al.*, 2007). Our data set plot in the same range as the several previous reports performed using various mantle-relevant compositions (bottom frame) (Kesson *et al.*, 1998; Murakami *et al.*, 2005; Auzende *et al.*, 2008; Sakai *et al.*, 2009; Irifune *et al.*, 2010; Narygina *et al.*, 2011; Sinmyo *et al.*, 2011; Nakajima *et al.*, 2012; Sinmyo and Hirose, 2013; Prescher *et al.*, 2014).



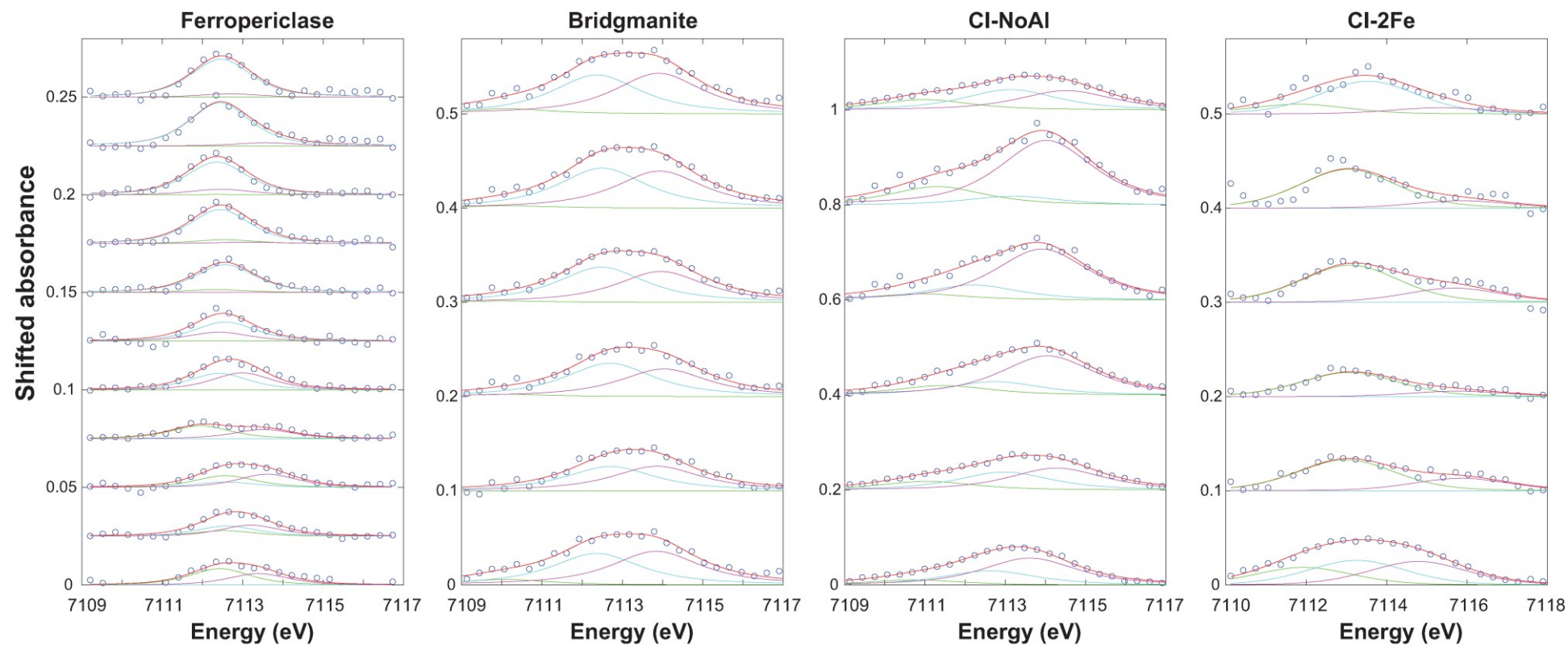


Figure S-4 Deconvolution of Fe-K pre-edges. Pre-edge features are located around 7110-7115 eV in the XANES spectra (Figs. S-1 and S-2). These features can be fitted by a sum of 3 contributions, plus a background. Then, the centroid positions are recalculated and compared with available references (Fig. 2). The pressure evolution of the energy position and intensity of pre-edge features in Fp and Bg can be used as a reference to discuss the redox state of Fe in our other samples containing a mixture of Fp and Bg.

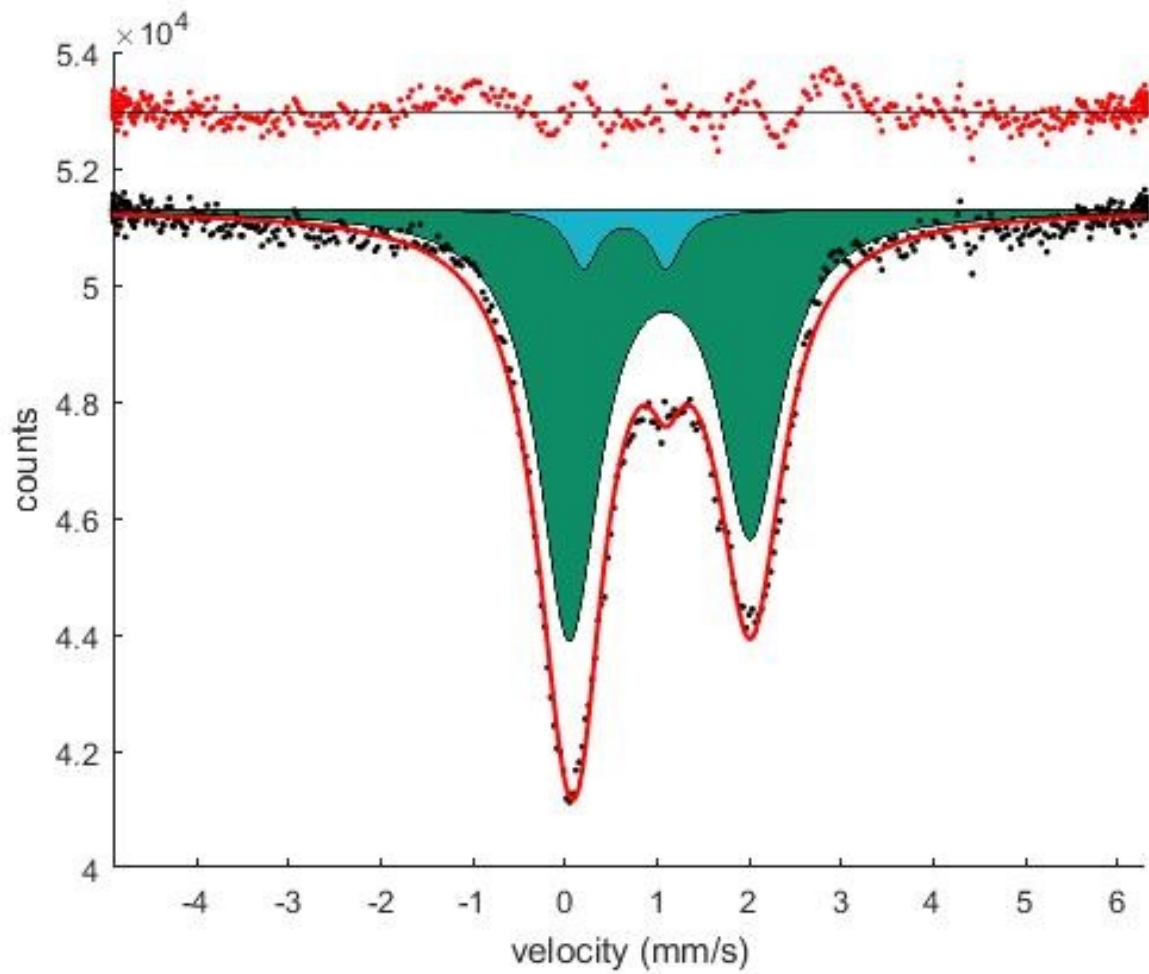


Figure S-5 Deconvolution of the SMS pattern of the glass starting material. The experimental spectrum (black dots) was recorded at 1 bar. According to previous works (Mao *et al.*, 2014; Murakami *et al.*, 2014), different contributions arise from high-spin Fe^{2+} (dark green doublet) and high-spin Fe^{3+} (light green doublet). The red line is the sum of these two contributions. The Fe^{3+} contribution points to $\#\text{Fe}^{3+}$ of 7.3 (0.5) %.

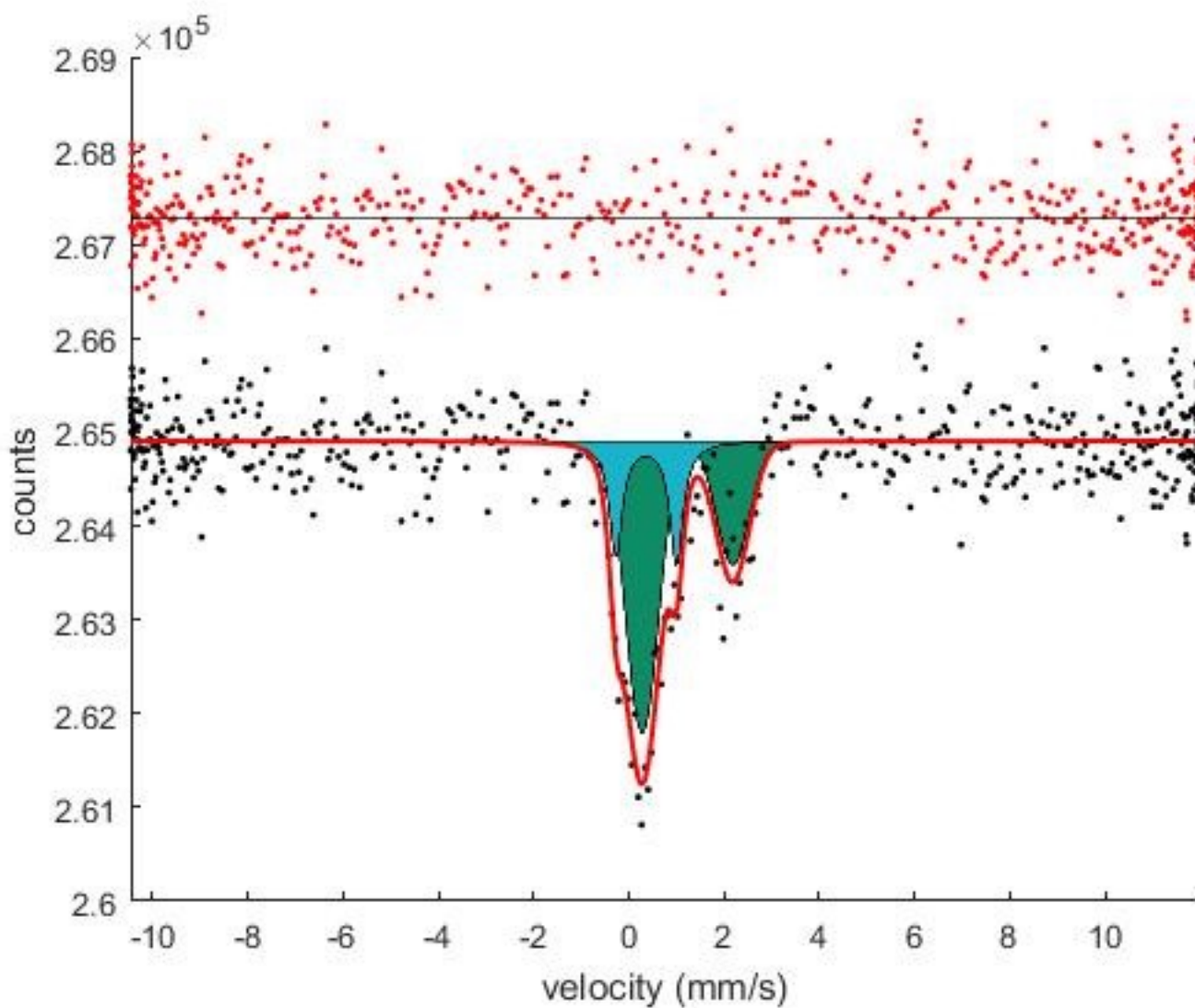


Figure S-6 SMS of the Bg reference compound (XANES). SMS measurement performed on the Bg sample recovered after the XANES experiments (Blue dots in Fig. 2). The spectrum presents two Fe contributions (Fe^{2+} HS and Fe^{3+} HS), yielding a $\#\text{Fe}^{3+}$ of 27(3) %.

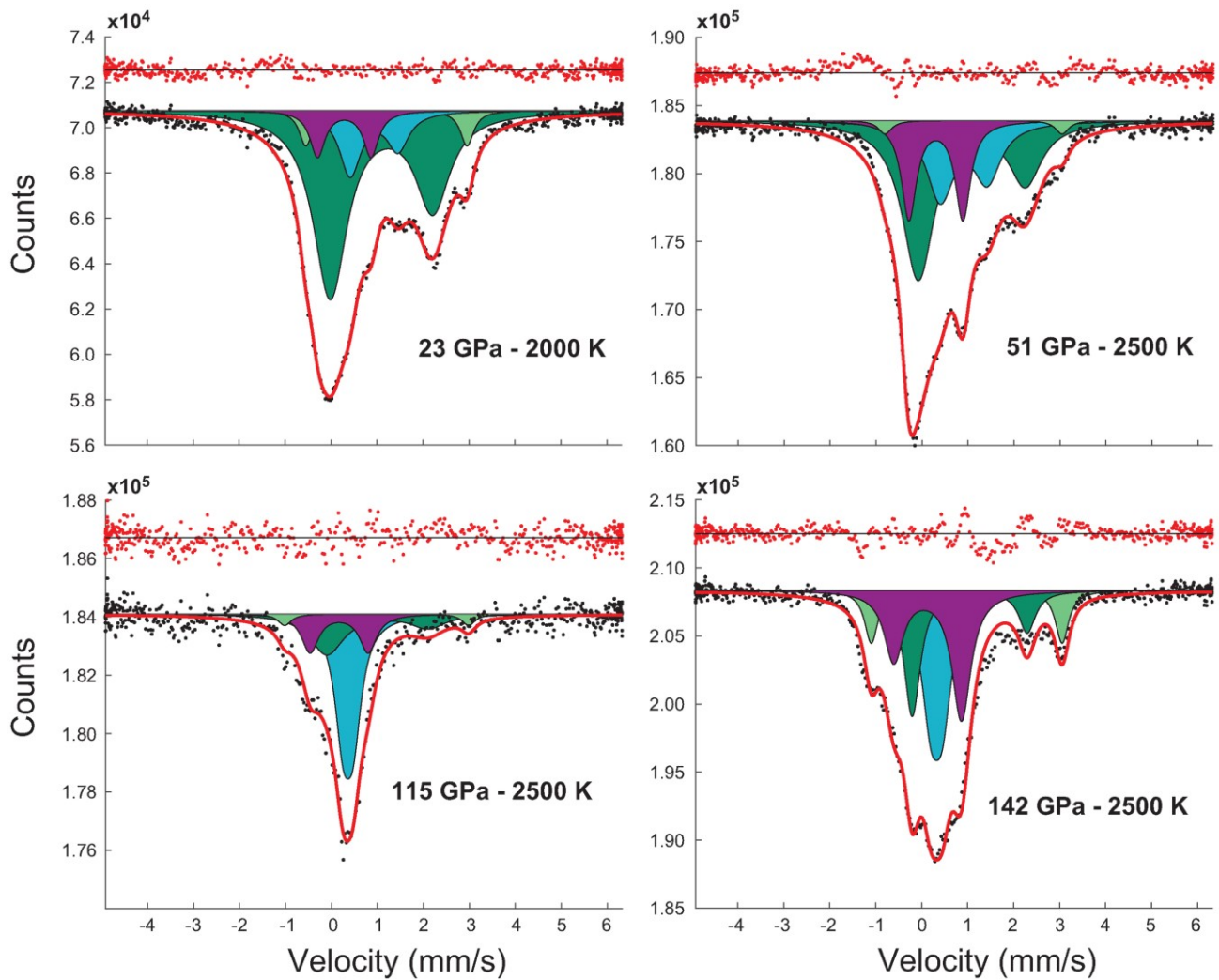


Figure S-7 Deconvolution of SMS patterns of our samples. Spectra were recorded at 300 K after synthesis at nominal pressures of 23 GPa (**upper-left**), 51 GPa (**upper-right**), 115 GPa (**lower-left**) and 142 GPa (**lower-right**). The five different contributions found in the samples are high-spin Fe^{2+} and low-spin Fe^{2+} in Fp (blue doublet and singlet, respectively), high-spin Fe^{2+} (dark green doublet), intermediate-spin Fe^{2+} (light green doublet) and high-spin Fe^{3+} (purple doublet) in Bg.

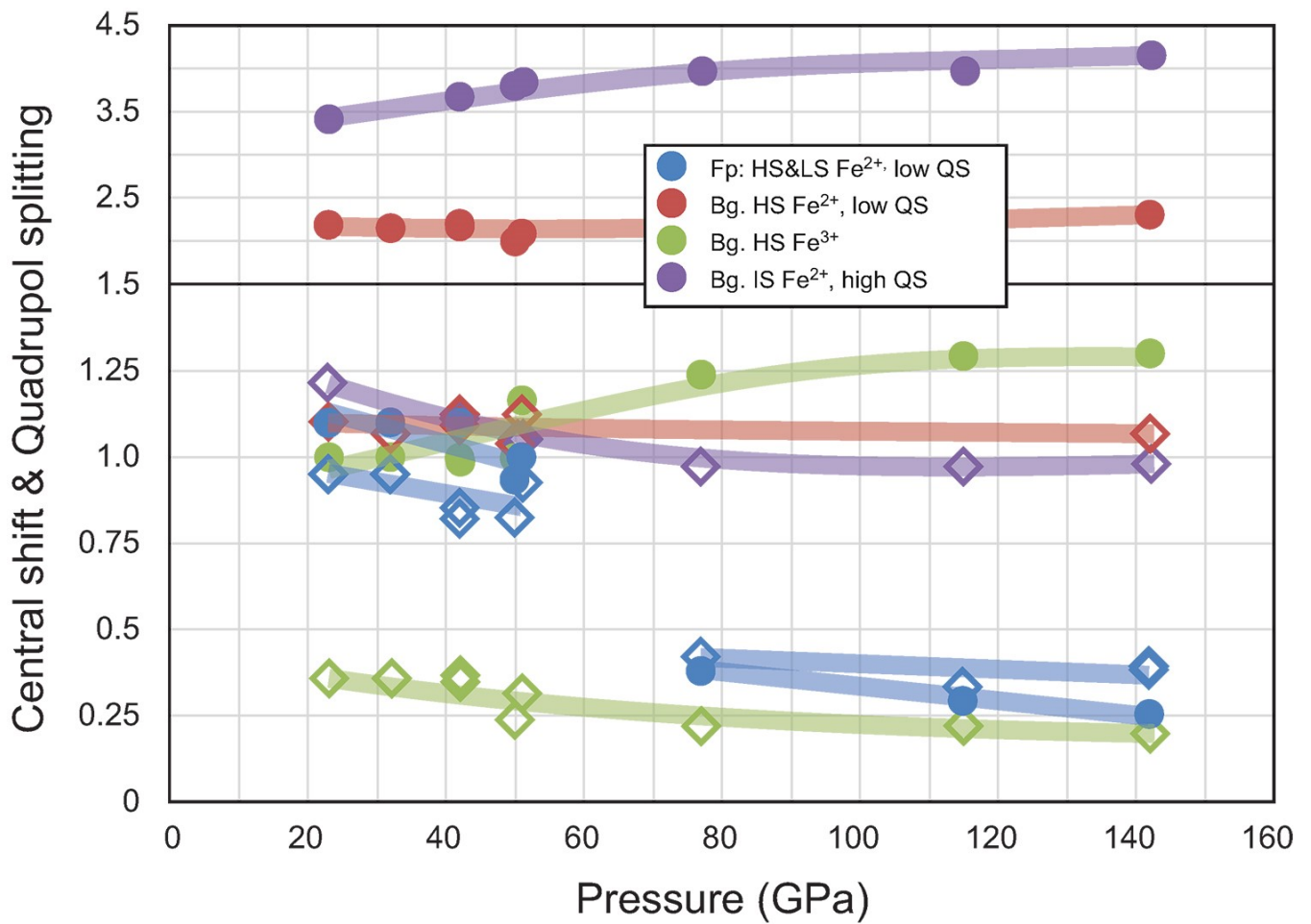


Figure S-8 Refined SMS parameters for transformed samples. CS (open lozenges) and QS (circles) are reported for the five Fe contributions: Two contributions for Fp are high-spin (low P) and low-spin (high P) Fe²⁺ (both reported in blue); three contributions for Bg are high-spin low-Q Fe²⁺ (red), high-spin Fe³⁺ (green) and intermediate-spin Fe²⁺ (purple). All QS and CS values were derived from previous works (McCammon *et al.*, 2008; Kantor *et al.*, 2009; Kuppenko *et al.*, 2014).



Supplementary Information References

- Andraut, D., Fiquet, G., Itié, J.P., Richet, P., Gillet, P., Häusermann, D., Hanfland, M. (1998) Thermal pressure in a laser-heated diamond-anvil cell: An x-ray diffraction study. *European Journal of Mineralogy* 10, 931-940.
- Andraut, D., Munoz, M., Bolfan-Casanova, N., Guignot, N., Perrillat, J.P., Aquilanti, G., Pascarelli, S. (2010) Experimental evidence for perovskite and post-perovskite coexistence throughout the whole D' region. *Earth and Planetary Science Letters* 293, 90-96.
- Auzende, A.-L., Badro, J., Ryerson, F.J., Weber, P.K., Fallon, T.J., Addab, A., Siebert, J., Fiquet, G. (2008) Element partitioning between magnesium silicate perovskite and ferropericlase: New insights into bulk lower-mantle geochemistry. *Earth and Planetary Science Letters* 269, 164-174.
- Badro, J., Fiquet, G., Guyot, F., Rueff, J.P., Struzhkin, V.V., Vanko, G., Monaco, G. (2003) Iron partitioning in Earth's mantle: Toward a deep lower mantle discontinuity. *Science* 300, 789-791.
- Badro, J., Rueff, J.P., Vanko, G., Monaco, G., Fiquet, G., Guyot, F. (2004) Electronic transitions in perovskite: possible nonconvecting layers in the lower mantle. *Science* 305, 383-386.
- Boujibar, A., Bolfan-Casanova, N., Andraut, D., Bouhifd, M.A., Trcera, N. (2016) Incorporation of Fe²⁺ and Fe³⁺ in bridgmanite during magma ocean crystallization. *American Mineralogist* 101, 1560-1570.
- Fei, Y.W., Zhang, L., Corgne, A., Watson, H., Ricolleau, A., Meng, Y., Prakapenka, V. (2007) Spin transition and equations of state of (Mg, Fe)O solid solutions. *Geophysical Research Letters* 34.
- Hennet, L., Cristiglio, V., Kozaily, J., Pozdnyakova, I., Fischer, H.E., Bytchkov, A., Drewitt, J.W.E., Leydier, M., Thiaudiere, D., Gruner, S., Brassamin, S., Zanghi, D., Cuello, G.J., Koza, M., Magazu, S., Greaves, G.N., Price, D.L. (2011) Aerodynamic levitation and laser heating: Applications at synchrotron and neutron sources. *European Physical Journal-Special Topics* 196, 151-165.
- Irifune, T., Koizumi, T., Ando, J. (1996) An experimental study of the garnet-perovskite transformation in the system MgSiO₃-Mg₃Al₂Si₃O₁₂. *Physics of the Earth and Planetary Interiors* 96, 147-157.
- Irifune, T., Shinmei, T., McCammon, C.A., Miyajima, N., Rubie, D.C., Frost, D.J. (2010) Iron Partitioning and Density Changes of Pyrolite in Earth's Lower Mantle. *Science* 327, 193-195.
- Kantor, I., Dubrovinsky, L., McCammon, C., Steinle-Neumann, G., Kantor, A., Skorodumova, N., Pascarelli, S., Aquilanti, G. (2009) Short-range order and Fe clustering in Mg_{1-x}Fe_xO under high pressure. *Physical Review B* 80.
- Kesson, S.E., Fitz Gerald, J.D., Shelley, J.M. (1998) Mineralogy and dynamics of a pyrolite lower mantle. *Nature* 393, 252-255.
- Kupenko, I., Dubrovinsky, L., Dubrovinskaia, N., McCammon, C., Glazyrin, K., Bykova, E., Ballaran, T.B., Sinmyo, R., Chumakov, A.I., Potapkin, V., Kantor, A., Ruffer, R., Hanfland, M., Crichton, W., Merlini, M. (2012) Portable double-sided laser-heating system for Mossbauer spectroscopy and X-ray diffraction experiments at synchrotron facilities with diamond anvil cells. *Review of Scientific Instruments* 83.
- Kupenko, I., McCammon, C., Sinmyo, R., Cerantola, V., Potapkin, V., Chumakov, A.I., Kantor, A., Ruffer, R., Dubrovinsky, L. (2015) Oxidation state of the lower mantle: In situ observations of the iron electronic configuration in bridgmanite at extreme conditions. *Earth and Planetary Science Letters* 423, 78-86.
- Kupenko, I., McCammon, C., Sinmyo, R., Prescher, C., Chumakov, A.I., Kantor, A., Ruffer, R., Dubrovinsky, L. (2014) Electronic spin state of Fe,Al-containing MgSiO₃ perovskite at lower mantle conditions. *Lithos* 189, 167-172.
- Lin, J.F., Vanko, G., Jacobsen, S.D., Iota, V., Struzhkin, V.V., Prakapenka, V.B., Kuznetsov, A., Yoo, C.S. (2007) Spin transition zone in Earth's lower mantle. *Science* 317, 1740-1743.
- Mao, Z., Lin, J.F., Yang, J., Wu, J.J., Watson, H.C., Xiao, Y.M., Chow, P., Zhao, J.Y. (2014) Spin and valence states of iron in Al-bearing silicate glass at high pressures studied by synchrotron Mossbauer and X-ray emission spectroscopy. *American Mineralogist* 99, 415-423.
- McCammon, C., Kantor, I., Narygina, O., Rouquette, J., Ponkratz, U., Sergueev, I., Mezouar, M., Prakapenka, V., Dubrovinsky, L. (2008) Stable intermediate-spin ferrous iron in lower-mantle perovskite. *Nature Geoscience* 1, 684-687.
- McCammon, C.A. (1997) Perovskite as a possible sink for ferric iron in the lower mantle. *Nature* 387, 694-696.
- Muñoz, M., De Andrade, V., Vidal, O., Lewin, E., Pascarelli, S., Susini, J. (2006) Redox and speciation micro-mapping using dispersive X-ray absorption spectroscopy: Application to iron in chlorite mineral of a metamorphic rock thin section. *Geochemistry Geophysics Geosystems* 7, Q11020.
- Munoz, M., Pascarelli, S., Aquilanti, G., Narygina, O., Kurnosov, A., Dubrovinsky, L.S. (2008) Hyperspectral μ -XANES mapping in the diamond-anvil cell: analytical procedure applied to the decomposition of (Mg,Fe)-ringwoodite at the upper/lower mantle boundary. *High Pressure Research* 28, 665-673.
- Munoz, M., Vidal, O., Marcaillou, C., Pascarelli, S., Mathon, O., Farges, F. (2013) Iron oxidation state in phyllosilicate single crystals using Fe-K pre-edge and XANES spectroscopy: Effects of the linear polarization of the synchrotron X-ray beam. *American Mineralogist* 98, 1187-1197.
- Murakami, M., Goncharov, A.F., Hirao, N., Masuda, R., Mitsui, T., Thomas, S.M., Bina, C.R. (2014) High-pressure radiative conductivity of dense silicate glasses with potential implications for dark magmas. *Nature Communications* 5.
- Murakami, M., Hirose, K., Sata, N., Ohishi, Y. (2005) Post-perovskite phase transition and mineral chemistry in the pyrolytic lowermost mantle. *Geophysical Research Letters* 32, L03304.
- Nakajima, Y., Frost, D.J., Rubie, D.C. (2012) Ferrous iron partitioning between magnesium silicate perovskite and ferropericlase and the composition of perovskite in the Earth's lower mantle. *Journal of Geophysical Research-Solid Earth* 117.
- Narygina, O., Dubrovinsky, L.S., Samuel, H., McCammon, C.A., Kantor, I.Y., Glazyrin, K., Pascarelli, S., Aquilanti, G., Prakapenka, V.B. (2011) Chemically homogeneous spin transition zone in Earth's lower mantle. *Physics of the Earth and Planetary Interiors* 185, 107-111.
- Narygina, O., Mattesini, M., Kantor, I., Pascarelli, S., Wu, X., Aquilanti, G., McCammon, C., Dubrovinsky, L. (2009) High-pressure experimental and computational XANES studies of (Mg,Fe)(Si,Al)O₃ perovskite and (Mg,Fe)O ferropericlase as in the Earth's lower mantle. *Physical Review B* 79.
- Piet, H., Badro, J., Nabiei, F., Dennenwaldt, T., Shim, S.H., Cantoni, M., Hebert, C., Gillet, P. (2016) Spin and valence dependence of iron partitioning in Earth's deep mantle. *Proceedings of the National Academy of Sciences of the United States of America* 113, 11127-11130.
- Potapkin, V., Chumakov, A.I., Smirnov, G.V., Celse, J.P., Ruffer, R., McCammon, C., Dubrovinsky, L. (2012) The Fe-57 Synchrotron Mossbauer Source at the ESRF. *Journal of Synchrotron Radiation* 19, 559-569.
- Prescher, C., Langenhorst, F., Dubrovinsky, L.S., Prakapenka, V.B., Miyajima, N. (2014) The effect of Fe spin crossovers on its partitioning behavior and oxidation state in a pyrolytic Earth's lower mantle system. *Earth and Planetary Science Letters* 399, 86-91.
- Prescher, C., McCammon, C., Dubrovinsky, L. (2012) MossA: a program for analyzing energy-domain Mossbauer spectra from conventional and synchrotron sources. *Journal of Applied Crystallography* 45, 329-331.
- Sakai, T., Ohtani, E., Terasaki, H., Sawada, N., Kobayashi, Y., Miyahara, M., Nishijima, M., Hirao, N., Ohishi, Y., Kikegawa, T. (2009) Fe-Mg partitioning between perovskite and ferropericlase in the lower mantle. *American Mineralogist* 94, 921-925.



- Shim, S.-H., Grocholski, B., Ye, Y., Alp, E.E., Xu, S., Morgan, D., Meng, Y., Prakapenka, V.B. (2017) Stability of ferrous-iron-rich bridgmanite under reducing midmantle conditions. *Proceedings of the National Academy of Sciences of the United States of America* 114, 6468-6473.
- Sinmyo, R., Hirose, K. (2013) Iron partitioning in pyrolitic lower mantle. *Physics and Chemistry of Minerals* 40, 107-113.
- Sinmyo, R., Hirose, K., Muto, S., Ohishi, Y., Akira, Y. (2011) The valence state and partitioning of iron in the Earth's lowermost mantle. *Journal of Physical Research* In Press.
- Wilke, M., Farges, F., Petit, P.E., Brown, J.G.E., Martin, F. (2001) Oxidation state and coordination of Fe in minerals: An Fe K-XANES spectroscopic study. *American Mineralogist* 86, 714-730.
- Wood, B.J., Rubie, D.C. (1996) The effect of alumina on phase transformations at the 660-kilometer discontinuity from Fe-Mg partitioning experiments. *Science* 273, 1522-1524.

